Journal of Materials Chemistry A

PAPER

View Article Online
View Journal | View Issue

CrossMark click for updates

Cite this: J. Mater. Chem. A, 2017, 5, 739

Control of preferred orientation with slow crystallization for carbon-based mesoscopic perovskite solar cells attaining efficiency 15%†

Cheng-Min Tsai, Guan-Wei Wu, Sudhakar Narra, Hung-Ming Chang, Nayantara Mohanta, Hui-Ping Wu, Chien-Lung Wang and Eric Wei-Guang Diau*

Received 18th October 2016
Accepted 24th November 2016

DOI: 10.1039/c6ta09036b

www.rsc.org/MaterialsA

To produce mesoscopic carbon-electrode-based solar cells free of a hole-conduction layer, we developed a simple one-step drop-cast method (temperature 20 °C, relative humidity 50%) to grow uniform and compact perovskite nanocrystals *via* slow crystallization (SC). X-ray diffraction (XRD) results indicated that perovskite nanocrystals produced inside the mesoporous $TiO_2/Al_2O_3/C$ layers according to our SC approach with *N*-methyl-2-pyrrolidone (NMP) as a precursor solvent showed a preferred orientation at facet (004) with large crystalline grains, whereas those produced with other solvents or *via* thermal annealing (TA) methods showed greater intensity at facet (220) with small crystals. After the SC (NMP) procedure was completed, additional TA treatment would change the preferred orientation from (004) back to facet (220), which would break the connectivity and lose the uniformity of the crystals, causing the grains to become significantly smaller. Transient photoluminescence (PL) decay profiles of the SC devices made with four precursor solvents, NMP, γ-butyrolactone (GBL), dimethylformamide (DMF) and dimethyl sulfoxide (DMSO), were recorded to show the trend of charge separation kinetics of the perovskite crystals inside the mesoporous films, which is consistent with the trend of the corresponding device performance showing the same order. The SC (NMP) device attained the best efficiency of power conversion (PCE), 15.0%, with average value (13.9 ± 0.5%), which is much superior to those devices from either the traditional one-step TA (DMF) method (5.2 ± 1.0%) or the traditional sequential TA method (10.1 ± 0.7%). This work emphasizes the significance of the control of preferred orientation of perovskite nanocrystals using the SC approach, to obtain high-performance carbon-based mesoscopic solar cells with excellent reproducibility and stability.

Introduction

Because those devices have excellent photovoltaic properties and enable cheap fabrication, organic–inorganic hybrid perovskite solar cells attract much attention.[1–3] Miyasaka and co-workers developed the first perovskite solar cell (PSC) based on dye-sensitized solar cells (DSSCs) with a mesoporous film structure and a liquid-type electrolyte.[4] Various approaches to fabricate uniform perovskite films with fewer defects for all-solid-state PSCs were then reported,[5–11] but the performance and enduring stability of the devices became a critical issue for the commercialization of these PSCs.[12] An approach to overcome the stability problem is to avoid the use of an organic layer as a hole-transport material (HTM) for the device,[13–16] but the cell performance without a HTM layer is typically inferior to the one with a HTM layer. Furthermore, back contact electrodes using a film of noble metal such as Au or Ag are expensive and require energy-intensive vacuum-evaporation techniques that impose further limitations on mass production. In 1996, Grätzel and co-workers demonstrated the use of graphite and a carbon-black composite as a cost-effective alternative to replace noble-metal counter electrodes in DSSCs.[17] In 2013, Han and co-workers applied a similar idea to fabricate a HTM-free PSC with a three-layer film configuration, $TiO_2/ZrO_2/C$, and obtained efficiency 6.6% of power conversion (PCE).[18] Thereafter, intensive investigations were initiated to fabricate carbon-based PSC devices using either a two-step sequential method or a one-step approach with dimethylformamide (DMF) as the precursor solvent,[19–27] but both methods required post-treatment for the crystal growth *via* thermal annealing (TA) at temperature 70–100 °C.

In previous work,[28] we developed a solvent-extraction method of crystal growth (SECG) to generate dense and uniform perovskite crystals in a mesoporous $TiO_2/Al_2O_3/C$ film. We used *N*-methyl-2-pyrrolidone (NMP) as a precursor solvent for perovskite infiltration, followed by the use of diethyl ether as

Department of Applied Chemistry, Institute of Molecular Science, National Chiao Tung University, No. 1001, Ta-Hsueh Rd., Hsinchu 30010, Taiwan. E-mail: diau@mail.nctu.edu.tw; Fax: +886-03-572-3764

† Electronic supplementary information (ESI) available. See DOI: 10.1039/c6ta09036b

a second solvent to extract the NMP inside the mesoporous film. Slow crystallization (SC) for the crystal growth, duration 5 days, raised the device performance to attain a PCE of 12.3%. In the present work, we found that the solvent extraction is an unnecessary step and that the SC approach works only for NMP, to attain a remarkable PCE of 15.0% for carbon-based PSCs. In contrast, SC failed for other commonly used solvents such as DMF, γ-butyrolactone (GBL) and dimethyl sulfoxide (DMSO). X-ray diffraction (XRD) measurements showed that the preferred orientation at facet (004) is an important factor to grow dense and uniformly close-packed perovskite nanocrystals with large crystals and enhanced photovoltaic performance. We demonstrate that the SC method using NMP as a solvent is an effective one-step approach for the fabrication of hole-conductor-free carbon-based perovskite solar cells, yielding device performance and reproducibility much superior to those fabricated using the traditional one-step and sequential TA methods.

Results and discussion

Fig. 1 shows the device configuration, energy levels and mechanism of crystal formation by the SC (NMP) method. The carbon-based devices were prepared according to a procedure reported elsewhere.[28] The images from an optical microscope (OM) (Fig. 1) show clearly the subsequent steps of crystal formation. After infiltration, nucleation began at 24 h; crystallization then proceeded with larger crystals at 48 h. The large crystal grains merged together at 72 h; the crystallization was eventually completed at 120 h. Our slow crystallization is a unique approach to grow dense and uniform perovskite nanocrystals for mesoporous carbon-based PSCs in air; the effects of both temperature (10, 20 and 30 °C) and relative humidity (30, 50 and 70%) were tested in a controlled chamber; the corresponding images of film formation and photovoltaic performance appear in Fig. S1–S6, Tables S1 and S2, ESI.† The best experimental conditions were temperature 20 °C and relative humidity 50%, for which the device performance exceeded 14%.

Fig. 2a shows current–voltage curves of the SC (NMP) devices at varied periods of crystal growth from 0 to 120 h; the corresponding IPCE spectrum at 120 h is shown in Fig. 2b, and the pertinent photovoltaic parameters are summarized in Table S3, ESI.† The photovoltaic performance gradually improved when the perovskite crystals continued to grow while the NMP solvent gradually evaporated from the mesoporous films. When the SC procedure was completed at 120 h, we obtained the best photovoltaic performance, with J_{SC}/mA cm^{-2} 22.43, V_{OC}/mV 893, FF 0.747 and PCE/% 15.0 (Fig. 2a), which is the best result for a carbon-electrode perovskite solar cell prepared by a simple one-step method.

We applied X-ray crystallographic analysis to test the extent of crystallization and the crystal phases of the perovskite grown using our SC method. Fig. 3a shows the XRD patterns of the perovskite films prepared by the SC (NMP) method at growth periods 0–120 h. Initially (0 h), no crystal was formed; no XRD

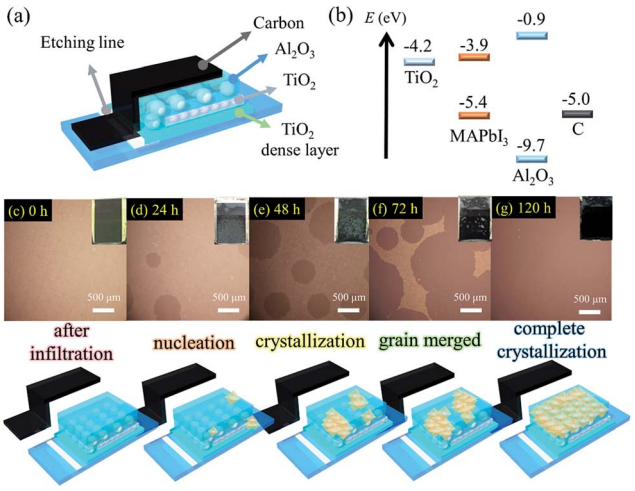

Fig. 1 Schematic illustration of the architecture of a carbon-based mesoscopic perovskite device (a), energy levels (b) of each component and a mechanism for the slow crystallization with NMP as the solvent at temperature 20 °C and relative humidity 50%; the corresponding OM images at varied crystal growth periods are indicated from (c) to (g).

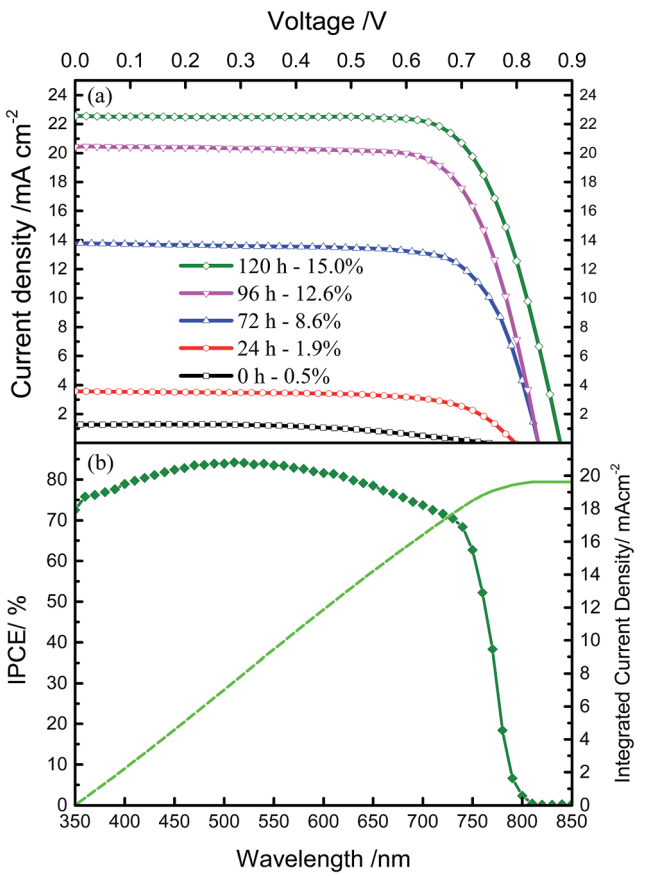

Fig. 2 (a) Current–voltage characteristics of SC devices prepared with NMP (active area 0.09 cm^2) under AM 1.5 G one-sun irradiation; the corresponding photovoltaic parameters are shown in Table S3.† (b) IPCE and integrated current density of the SC (NMP) device at period 120 h of crystal growth.

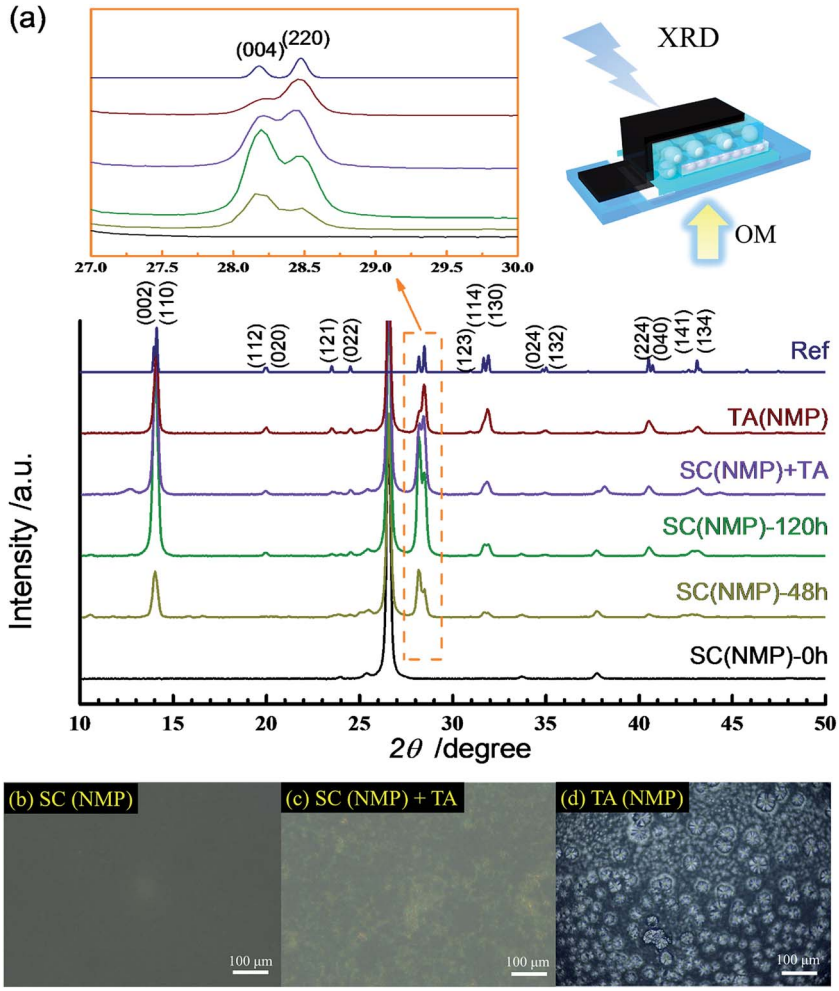

Fig. 3 (a) X-ray diffraction (XRD) patterns of devices deposited on mesoporous FTO/TiO_2/Al_2O_3/C substrates prepared by SC (NMP) methods initially (0 h), and at 48 h and 120 h. The fourth trace from the bottom shows the XRD pattern of a SC (NMP)-120 h sample with additional thermal annealing at 70 °C for 48 h; the fifth trace from the bottom pertains to a perovskite film produced with direct thermal annealing at 70 °C for 30 min, TA (NMP). The top trace is the powder XRD reference pattern of perovskite reproduced from the ICSD data base (code number 250739). The left inset of (a) highlights the variation of the preferred orientations at the (004) and (220) facets; the right inset of (a) shows the directions for the XRD (from the carbon side) and the OM (from the glass side) measurements. OM images of SC (NMP)-120 h, SC (NMP) + TA and TA (NMP) samples are shown in (b), (c) and (d), respectively. The scale bars in the corner of each image represent 100 μm.

signal was observed except an intense background signal at 26.5° due to the contribution of the carbon electrode. When the perovskite crystals formed, all samples adopted a tetragonal structure and exhibited two characteristic signals about 28° corresponding to facets (004) and (220), as highlighted in the dotted box in Fig. 3a. After growth for 48 h, SC (NMP)-48 h, crystallization proceeded (Fig. 1) with the preferred orientation at facet (004). The crystallinity of the perovskite improved further at 120 h, SC (NMP)-120 h, with a stronger preferred orientation for facet (004) than for facet (220). In a reference powder-diffraction sample (Ref) with randomly oriented crystals, facet (220) exhibits an intensity greater than that of facet (004), but, for the SC (NMP) samples, the (004) signal shows a greater intensity, signifying that the crystals produced by the SC (NMP) method had a preferred orientation at facet (004).[29] A preferred orientation is commonly observed when crystals are grown inside rolled samples, tablets or thin films because of their mechanical properties or larger crystal grains that connect with each other in a particular orientation, unlike powders that show randomly oriented crystal domains.[29]

Shown in images from the OM in Fig. 3b and from a scanning electron microscope (SEM) in Fig. S2b, ESI,† the perovskite crystals that grew completely through the mesoporous TiO_2/Al_2O_3 layers by the SC (NMP) method show large crystals without a clear grain boundary, which might be the reason for the preferred orientation enhanced at facet (004). To prove that this preferred orientation came from large and well-connected perovskite crystals, we heated the SC (NMP)-120 h sample at 70 °C for 48 h, SC (NMP) + TA; the crystallinity of this perovskite was degraded with a signal at (220) more intense than at (004). Post-TA treatment of the SC (NMP)-120 h sample led to decomposition of the perovskite because PbI_2 in a trace proportion was observed at ~13°, which reasonably accounts for the loss of connectivity of the crystal grains; this observation

is an explanation of the change of preferred orientation from (004) to (220) to show a disparate diffraction pattern. When the perovskite crystals were prepared with TA (NMP) directly, the diffraction intensity was more intense at the (220) signal, which is a crystallographic feature the same as that in the powder perovskite sample (labeled as Ref in Fig. 3a) with random crystal orientation. The above results are consistent with the OM images shown in Fig. 3b–d.

For the carbon-electrode PSC, the XRD patterns of our TA (NMP) device are consistent with those reported by Mei *et al.*[19] and those reported by Wang *et al.*[24] using the traditional one-step TA method (DMF), as well as those reported by Cao *et al.*[25] using a traditional two-step (sequential) method; both traditional methods for carbon-based PSCs showed the same preferred orientation at facet (220). A similar phenomenon was found for PSCs of other types with crystallization of perovskite films according to the TA methods.[30–32] We found, however, one exception for the perovskite film produced using the thermal deposition method under vacuum for an inverted planar PSC.[33] In that approach, the perovskite nanocrystals were slowly deposited layer by layer so that the crystal grains could connect well with each other. The XRD patterns thus showed greater intensity for the (004) signal than for the (220) signal, which is consistent with our SC approach using NMP as the precursor solvent.

The control of the preferred orientations for perovskite crystals was reported by Docampo *et al.*[34] and by Koza *et al.*,[35] for which the XRD intensity of the (004) facet was found to decrease when the perovskite crystals were produced at a higher temperature. Hence, at higher reaction temperatures, the crystals were preferentially oriented with the long axis parallel to the substrate at the (220) facet. Under the low-temperature

Table 1 Lattice parameters obtained from TOPAS simulations as shown in Fig. S7

Device	S.G.	a/Å	b/Å	c/Å	$\alpha = \beta = \gamma$/deg	Volume/Å^3	Fitted crystal size/nm
SC (NMP)	*I4cm*	8.862	8.862	12.658	90	994.10	81.4
SC (NMP) + TA	*I4cm*	8.871	8.871	12.655	90	995.88	59.3
TA (NMP)	*I4cm*	8.865	8.865	12.656	90	994.61	49.4

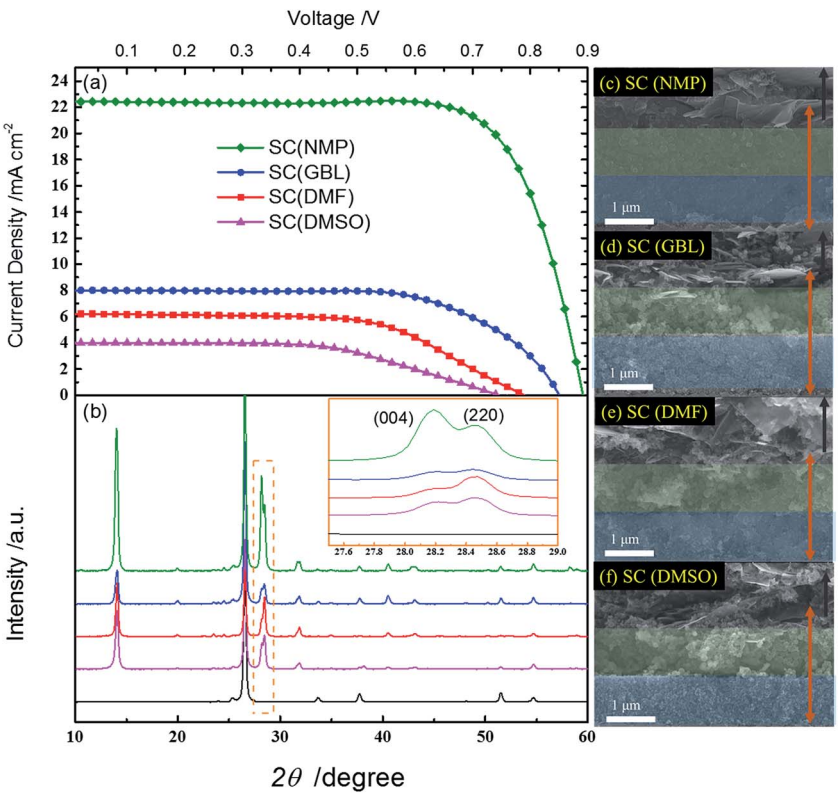

Fig. 4 (a) Current–voltage characteristics of SC devices prepared with four solvents deposited on mesoporous FTO/TiO_2/Al_2O_3/C substrates under AM 1.5 G one-sun irradiation; the corresponding photovoltaic parameters are specified in Table 2. (b) XRD patterns of the corresponding devices as indicated; the inset of (b) highlights the preferred orientations of the four devices in the dotted box region. The corresponding SEM side-view images shown in (c) to (f) represent the devices made with NMP, GBL, DMF and DMSO solvents, respectively; the scale bar represents 1 μm. Three layers (TiO_2, Al_2O_3 and carbon) in the SEM images are highlighted in separate colours, with orange arrows representing the growth levels of the perovskite crystals.

conditions, however, the XRD intensity of the (004) facet would increase, which indicates that the crystals were grown preferentially oriented with the long axis perpendicular to the substrate.[34,35] Their results are thus consistent with our results obtained from the SC method, for which crystals were formed slowly at the low temperature to give the preferred orientation with enhanced XRD at the (004) facet. The key to control the preferred orientations is the rate of the crystal growth rather than the temperature, but a smaller rate of crystal growth can be achieved at a lower temperature.

Those XRD patterns were simulated using TOPAS software; the results are shown in Fig. S7, ESI† and summarized in Table 1. Our results apparently show that the SC (NMP) approach generates crystals larger than those from a conventional TA (NMP) method, and confirm that the post-TA treatment breaks the crystal grain connectivity to produce a smaller crystal. We thus discovered that the dense and uniform perovskite crystals in carbon-based mesoscopic solar cells should have a preferred orientation signal stronger at (004) rather than at (220).

Fig. 4 shows photovoltaic characterization, XRD and SEM side-view images of the carbon-based PSC fabricated by the SC method and four solvents – NMP, GBL, DMF and DMSO; the corresponding photovoltaic data are summarized in Table 2. Except the device fabricated using the NMP solvent, the devices exhibited poor photovoltaic performance. According to the SEM images shown in Fig. 4d–f, the perovskite films grown from the DMF, GBL and DMSO solvents included large voids and the grain connectivity was poor. Their XRD patterns thus showed a preferred orientation at the (220) signal, similar to those of the powder and TA samples. The XRD patterns were simulated with TOPAS software based on the ICSD data base (code number 250739); the fitted results are shown in Fig. S8, ESI;† the crystal parameters are summarized in Table 3. The fitted results show that the crystal grains from SC (NMP) were approximately twice as large as the others. The perovskite films fabricated using the NMP solvent clearly had superior morphology, pore-filling and grain connectivity to yield device performance much greater than the others. Large crystal grains with great connectivity and complete pore-filling through the TiO_2 and Al_2O_3 layers are critical factors that lead to high performance for the NMP devices.

As mentioned above, the key to obtain high-quality crystals by the SC method is to control the rate of crystallization; the physical property of the solvent is thus important. One characteristic is the small vapour pressure of NMP (0.29 Torr at 25 °C), which is much less than that for other precursor solvents, DMSO (0.42 Torr), GBL (1.5 Torr) and DMF (2.7 Torr). The vapour pressure of DMSO is also small, but DMSO acts as a Lewis base to form an adduct with PbI_2, which might require increasing the temperature for crystallization to proceed more effectively.[10] NMP thus becomes the best candidate to assist the slow crystallization with the preferred orientation to produce uniform, dense and close-packed crystals with large grains and connectivity inside the mesoporous metal-oxide layers for the superior photovoltaic performance observed herein.

We have measured photoluminescence (PL) transient decays using time-correlated single-photon counting (TCSPC) to investigate the charge-transfer kinetics and the extent of charge separation in relation to the film morphology and device performance shown in Fig. 4. The lifetimes of perovskite have been reported over a broad time scale depending on many factors such as crystallite size,[36] excitation power,[37–39] morphology[40–42] and film configuration. In the present work, perovskite crystals of varied types were crystallized inside the mesoporous layers with an identical film configuration; the measured time coefficients hence reflect the intrinsic property of varied perovskite nanocrystals generated with the four SC solvents applied herein. Under the same experimental conditions for the TCSPC measurements, the non-radiative relaxation would be accelerated when charge separation of perovskite nanocrystals inside the mesoporous layers became more efficient, resulting in quenching of PL and decreased lifetimes.

Fig. 5 shows time-resolved PL decays for devices of these four kinds. All PL transients were fitted with a bi-exponential decay function; the corresponding lifetimes and relative amplitudes are summarized in Table 4. In our previous investigation using the SECG approach,[28] the two decay components (τ_1 and τ_2) were assigned to the non-radiative relaxations due to charge separation and surface-defect relaxation, respectively, but in the present work we found that charge separation should contribute to both decay components: the first decay component (τ_1) might be due to the electron injection at the

Table 2 Photovoltaic parameters of SC devices with various solvents obtained from current–voltage curves shown in Fig. 4a. All devices were investigated under AM 1.5 G one-sun irradiation with active area 0.09 cm^2

SC solvent	J_{SC}/mA cm^{-2}	V_{OC}/mV	FF	η/%
NMP	22.43	893	0.75	15.0
GBL	8.01	853	0.66	4.5
DMF	6.20	789	0.60	2.9
DMSO	4.02	743	0.56	1.7

Table 3 Lattice parameters of SC devices obtained from TOPAS simulations as shown in Fig. S8

SC solvent	S.G.	a/Å	b/Å	c/Å	$\alpha = \beta = \gamma$/deg	Volume/$Å^3$	Fitted crystal size/nm
NMP	*I*4*cm*	8.862	8.862	12.658	90	994.10	81.4
GBL	*I*4*cm*	8.863	8.863	12.656	90	994.16	47.8
DMF	*I*4*cm*	8.867	8.867	12.691	90	997.81	44.5
DMSO	*I*4*cm*	8.867	8.867	12.659	90	995.30	43.9

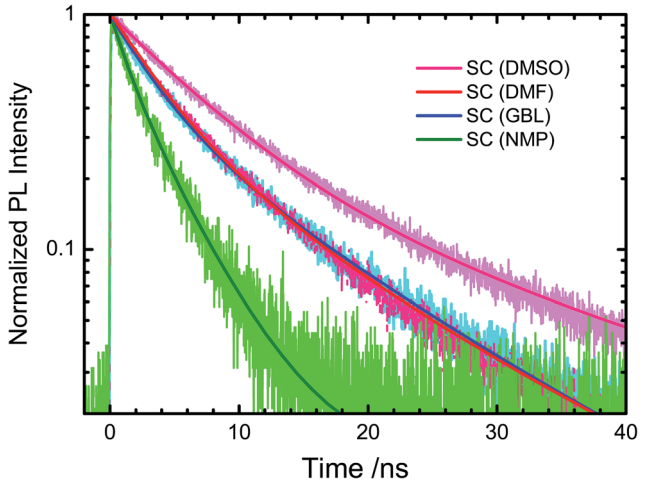

Fig. 5 Photoluminescence (PL) decays of carbon-based perovskite solar cells fabricated by the SC method with four precursor solvents showing kinetics of charge transfer and defect relaxation (excitation at 635 nm, probe at 770 nm).

Table 4 Lifetimes (relative amplitudes) of carbon-based perovskite solar cells with the perovskite layer synthesized according to slow crystallization (SC) of four solvents (excitation at 635 nm, probe at 770 nm)

Device	$\tau_1(A_1)$/ns	$\tau_2(A_2)$/ns	τ_{PL}[a]/ns
SC (NMP)	1.9 ± 0.1 (0.61)	5.1 ± 0.1 (0.39)	3.9 ± 0.1
SC (GBL)	3.4 ± 0.1 (0.64)	12.2 ± 0.3 (0.36)	9.1 ± 0.1
SC (DMF)	4.0 ± 0.1 (0.68)	12.5 ± 0.1 (0.32)	9.3 ± 0.2
SC (DMSO)	6.8 ± 0.1 (0.80)	25.4 ± 0.6 (0.20)	15.8 ± 0.4

[a] The average lifetime was calculated with this statistical definition: $\tau_{PL} = \frac{\sum A_i\tau_i^2}{\sum A_i\tau_i}$, in which lifetimes τ_i and corresponding amplitudes A_i of each component appear.

perovskite/TiO_2 interface; the second decay component (τ_2) is due to the defect-state relaxation as well as due to electron transfer from the bulk perovskite inside the mesoporous TiO_2 layer. This assignment is based on the fact that all other devices exhibited much slower relaxation than those of the SC (NMP) device because of the poor surface contact of the perovskite crystals inside the mesoporous films for other devices, as the side-view SEM images show in Fig. 4d–f. We found that the values of τ_1 display a trend with the order SC (NMP) < SC (GBL) < SC (DMF) < SC (DMSO), which is consistent with the corresponding device performance (Fig. 4 and Table 2) for which more rapid charge separation would give superior device performance. It shows also a similar trend for the values of τ_2 with the order SC (NMP) < SC (GBL) ~ SC (DMF) < SC (DMSO). The efficient charge separation in the SC (NMP) device is thus the evidence for its great device performance. Based on the results obtained from both SEM and PL transient-decay analysis, formation of dense and uniform perovskite crystals inside the mesoporous layers is clearly a necessary requirement for efficient charge separation to occur; this requirement is fulfilled for the SC (NMP) device to attain efficiency PCE = 15.0%; the poor PV performances of the other SC devices were due to their poor pore-filling inside the films that made the electron transfer from perovskite to TiO_2 inefficient as we observed from the transient PL measurements herein.

We compared the photovoltaic performance and the reproducibility of the carbon-based PSC devices fabricated by our SC method with other traditional TA methods (one-step and sequential). Fig. 6a shows the best photovoltaic performances with the photovoltaic parameters summarized in Table S4, ESI.† The histograms of devices of the three types are shown in Fig. 6b with the corresponding average values listed in Table 5. In general, TA methods use DMF as the precursor solvent, which gave a poor device performance using our SC method (Fig. 4) because the SC approach requires performance under a condition of small vapour pressure to generate compact crystals with the preferred orientation. The one-step TA method hence endowed the devices with a broad distribution of performance, with average PCE 5.2 ± 1.0%. The sequential method is a two-step approach but a TA treatment is also required, which alters the preferred orientation to become unfavourable for the mesoporous films. As a result, the sequential method also gave the

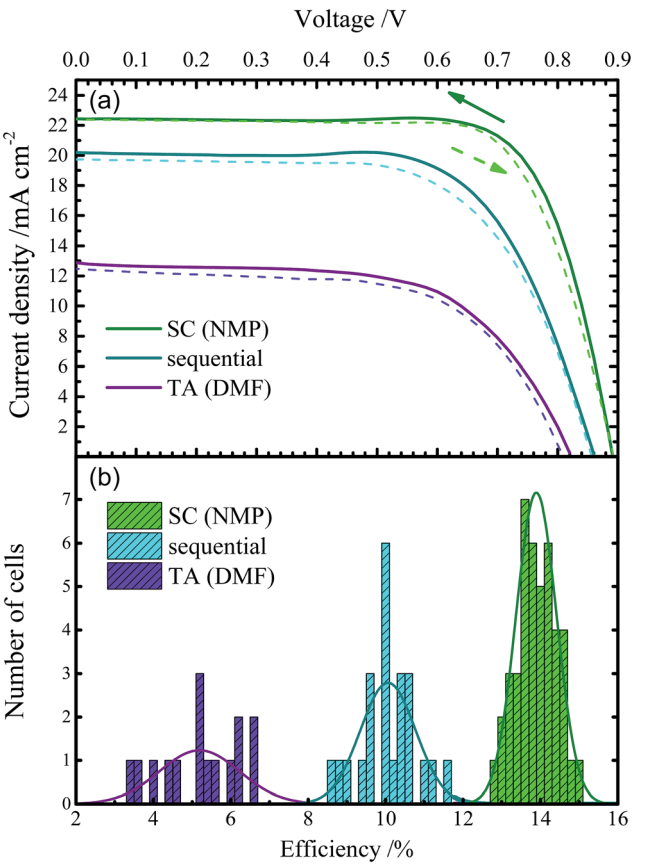

Fig. 6 Photovoltaic performance of devices fabricated according to one-step thermal annealing (DMF as the solvent), two-step sequential (DMF as the first solvent) and one-step slow crystallization (NMP as the solvent) methods showing (a) the best current–voltage characteristic with reverse (solid) and forward (dashed) scans and (b) histograms of PCE for devices of each type.

Table 5 Average photovoltaic parameters of devices obtained from histograms shown in Fig. 6b

Deposition method	J_{SC}/mA cm^{-2}	V_{OC}/mV	FF	η/%
TA (DMF)	10.18 ± 2.10	839 ± 36	0.611 ± 0.039	5.2 ± 1.0
Sequential	18.50 ± 1.21	826 ± 44	0.663 ± 0.030	10.1 ± 0.7
SC (NMP)	21.70 ± 0.82	876 ± 21	0.734 ± 0.021	13.9 ± 0.5

devices a broad distribution of performance with average PCE 10.1 ± 0.7%. In contrast, our SC (NMP) devices have a distribution of performance more narrow than the others and gave average PV performances with J_{SC}/mA cm^{-2} 21.70 ± 0.82, V_{OC}/mV 876 ± 21, FF 0.734 ± 0.021 and PCE/% 13.9 ± 0.5, which are remarkable for carbon-based PSCs with excellent intrinsic stability.[25] The SC (NMP) devices were stable when they were stored near 25 °C and relative humidity 50% for ~3000 h without encapsulation (Fig. S9, ESI†). Device performance would decay significantly when the cell was continuously under irradiation with sunlight, similar to the results of long-term stability reported for the carbon-based mesoscopic perovskite solar cells.[28]

Conclusion

Mesoscopic perovskite solar cells with a carbon layer as a counter electrode are free of air-sensitive organic hole conductors and rare and expensive metallic layers; they are hence promising as all-printable photovoltaic devices. In this work, we developed a simple one-step drop-casting slow-crystallization (SC) method to fabricate highly efficient carbon-based perovskite solar cells using NMP as a precursor solvent. The crystallization proceeded and became complete at growth period 120 h under the best experimental conditions (temperature 20 °C, relative humidity 50%) to generate dense and uniform perovskite crystals inside the mesoporous multilayer film; the TiO_2/Al_2O_3/C configuration was confirmed with SEM images. The XRD results indicate that the perovskite nanocrystals produced *via* our SC approach had a preferred orientation to show greater intensity at the (004) signal than at the (220) signal, whereas those produced by a rapid thermal-annealing (TA) method *via* either a one-step or a sequential approach would show crystals with the orientation at facet (220) similar to that obtained from the powder XRD data with randomly oriented crystals. Further post-TA treatment would break the grain connectivity to increase the intensity at (220) with smaller grains, confirming that our SC method is an effective approach to generate uniform and close-packed perovskite nanocrystals with large grains inside a mesoporous thin-film structure. Three other commonly used precursor solvents (DMF, GBL and DMSO) were tested using our SC approach but they all generated perovskite nanocrystals with poor device performance due to poor pore filling for the crystals with random orientation. The photoluminescence transients of these devices were recorded with the TCSPC technique with excitation at 635 nm and probe at 770 nm. The average lifetimes of the SC devices provide the rates of charge separation showing an order SC (NMP) > SC (GBL) > SC (DMF) > SC (DMSO), which is consistent with the corresponding device performance showing the same order. The best performance of the SC devices using the NMP solvent showed PCE 15.0% with a narrow distribution of performance that produced an average PCE 13.9 ± 0.5%, which is a remarkable record for printable mesoscopic carbon-based perovskite solar cells with excellent stability and reproducibility.

Experiments

Materials

Methylammonium iodide (MAI) was synthesized and purified according to procedures reported elsewhere.[28] PbI_2 (99.98%, Alfa Aesar), isopropanol (IPA, anhydrous, Aldrich), *N*-methyl-2-pyrrolidone (NMP, anhydrous, Aldrich), dimethyl sulfoxide (DMSO, anhydrous, Aldrich), dimethylformamide (DMF, anhydrous, Aldrich) and γ-butyrolactone (GBL, anhydrous, Aldrich) were used without further purification. The perovskite ($MAPbI_3$) precursor solution was prepared with MAI (175 mg) and the PbI_2 mixture (507 mg) in equimolar proportions in a solvent (1.0 mL). The experimental procedures to prepare TiO_2, Al_2O_3 and carbon pastes used in our work to prepare the corresponding mesoporous layers are reported elsewhere.[28]

Preparation of an electrode and devices

A TiO_2 compact layer (thickness 50 nm) was first deposited on etched FTO glass by a thermal spraying method. A mesoporous TiO_2 layer (thickness 1 μm) was then screen-printed on top of the compact layer. After that, mesoscopic Al_2O_3 (thickness 1 μm) and mesoscopic carbon (thickness 10 μm) layers were coated onto the TiO_2 layer *via* screen printing. The substrate was annealed at 400 °C for 30 min. After annealing, the precursor solution (3.0 μL) with solvent NMP, DMSO, DMF or GBL under the same conditions was dropped onto the electrode film as prepared (active area 0.5 cm^2); the crystal growth then proceeded inside the chamber (DBL45, Deng Ying) for which the temperature (from 0 to 80 °C) and relative humidity (from 30% to 98%) were well controlled.

Characterization of materials

The crystallographic structure of the perovskite films was obtained with X-ray diffraction (XRD, Bruker D8-Advance, Cu K_α radiation); the samples were prepared according to the same process as the solar-cell devices. The crystal structures were simulated with TOPAS software, version 4.2, using a cif file from ICSD data base code number 250739 with space group *I*4*cm*. The side view and morphology of the devices were examined with a cold-field-emission scanning electron microscope (FESEM, SU8010, Hitachi) and an optical microscope (OM, BX51, Olympus). The PL transients were recorded with a time-correlated single-photon counting (TCSPC) system (Fluotime 200, PicoQuant) with excitation *via* a vertically polarized 635 nm picosecond pulsed-diode laser (LDH-635, PicoQuant, FWHM ~ 70 ps) controlled with a picosecond pulsed laser driver

(PDL200-B, PicoQuant). The repetition rate of the laser is 4 MHz. The laser fluence used for excitation was ~64 nJ cm^{-2}. The PL emitted from the sample was collected with a lens at right angle. An iris served to attenuate the intensity of the detected signal; the polarization of the detected PL relative to the excitation laser pulse was set at 54.7° (magic angle) with a polarizer. A double monochromator was used to compensate the group-velocity dispersion of the signal and to select the detection wavelength. The grating of the double monochromator was set to 770 nm to select emission from the maximum of the PL. A micro-channel plate photomultiplier (MCP-PMT, R3809U-57, Hamamatsu) was connected to a computer with a TCSPC-module (SPC-630, Becker and Hickl) card for data acquisition.

Photovoltaic characterization

The photovoltaic performance of the devices was characterized with a solar simulator (AM 1.5G, XES-40S1, SAN-EI); the current–voltage scan rate was fixed at 0.07 V s^{-1}; the solar simulator was calibrated with a standard Si reference cell (Oriel, PN 91150V, VLSI standards). A metal mask (area 0.09 cm^2) was used in measurement of the IV curves of the devices. The incident efficiency spectra of the conversion of monochromatic photons to current (IPCE) of the devices were recorded with a system consisting of a Xe lamp (A-1010, PTi, 150 W), a monochromator (PTi, 1200 g mm^{-1} blazed at 500 nm) and a source meter (Keithley 2400). A standard Si photodiode (S1337-1012BQ, Hamamatsu) served as a reference for the calibration of the power density of the light source at each wavelength for the IPCE measurements.

Acknowledgements

The Ministry of Science and Technology (MOST) of Taiwan supported this work under contracts MOST105-2119-M-009-011-MY3 and MOST 104-2119-M-009-001.

References

1 P. Gao, M. Grätzel and M. K. Nazeeruddin, *Energy Environ. Sci.*, 2014, **7**, 2448–2463.
2 J. H. Rhee, C.-C. Chung and E. W.-G. Diau, *NPG Asia Mater.*, 2013, **5**, e68.
3 N.-G. Park, *Mater. Today*, 2015, **18**, 65–72.
4 A. Kojima, K. Teshima, Y. Shirai and T. Miyasaka, *J. Am. Chem. Soc.*, 2009, **131**, 6050–6051.
5 H. S. Kim, C. R. Lee, J. H. Im, K. B. Lee, T. Moehl, A. Marchioro, S. J. Moon, R. Humphry-Baker, J. H. Yum, J. E. Moser, M. Grätzel and N.-G. Park, *Sci. Rep.*, 2012, **2**, 591.
6 M. M. Lee, J. Teuscher, T. Miyasaka, T. N. Murakami and H. J. Snaith, *Science*, 2012, **338**, 643–647.
7 J. Burschka, N. Pellet, S. J. Moon, R. Humphry-Baker, P. Gao, M. K. Nazeeruddin and M. Grätzel, *Nature*, 2013, **499**, 316–319.
8 M. Liu, M. B. Johnston and H. J. Snaith, *Nature*, 2013, **501**, 395–398.
9 H. Zhou, Q. Chen, G. Li, S. Luo, T.-B. Song, H.-S. Duan, Z. Hong, J. You, Y. Liu and Y. Yang, *Science*, 2014, **345**, 542–546.
10 N. Ahn, D. Y. Son, I. H. Jang, S. M. Kang, M. Choi and N.-G. Park, *J. Am. Chem. Soc.*, 2015, **137**, 8696–8699.
11 W. S. Yang, J. H. Noh, N. J. Jeon, Y. C. Kim, S. Ryu, J. Seo and S. I. Seok, *Science*, 2015, **348**, 1234–1237.
12 G. Niu, X. Guo and L. Wang, *J. Mater. Chem. A*, 2015, **3**, 8970–8980.
13 L. Etgar, P. Gao, Z. Xue, Q. Peng, A. K. Chandiran, B. Liu, M. K. Nazeeruddin and M. Grätzel, *J. Am. Chem. Soc.*, 2012, **134**, 17396–17399.
14 Y. Xiao, G. Han, Y. Li, M. Li, Y. Chang and J. Wu, *J. Mater. Chem. A*, 2014, **2**, 16531–16537.
15 Y. Xiao, G. Han, Y. Li, M. Li and J. Wu, *J. Mater. Chem. A*, 2014, **2**, 16856–16862.
16 Y. Xiao, G. Han, Y. Chang, Y. Zhang, Y. Li and M. Li, *J. Power Sources*, 2015, **286**, 118–123.
17 A. Kay and M. Grätzel, *Sol. Energy Mater. Sol. Cells*, 1996, **44**, 99–117.
18 Z. Ku, Y. Rong, M. Xu, T. Liu and H. Han, *Sci. Rep.*, 2013, **3**, 3132.
19 A. Mei, X. Li, L. Liu, Z. Ku, T. Liu, Y. Rong, M. Xu, M. Hu, J. Chen, Y. Yang, M. Grätzel and H. Han, *Science*, 2014, **345**, 295–298.
20 K. Cao, Z. Zuo, J. Cui, Y. Shen, T. Moehl, S. M. Zakeeruddin, M. Grätzel and M. Wang, *Nano Energy*, 2015, **17**, 171–179.
21 L. Liu, A. Mei, T. Liu, P. Jiang, Y. Sheng, L. Zhang and H. Han, *J. Am. Chem. Soc.*, 2015, **137**, 1790–1793.
22 Z. Liu, M. Zhang, X. Xu, F. Cai, H. Yuan, L. Bu, W. Li, A. Zhu, Z. Zhao, M. Wang, Y.-B. Cheng and H. He, *J. Mater. Chem. A*, 2015, **3**, 24121–24127.
23 X. Xu, Z. Liu, Z. Zuo, M. Zhang, Z. Zhao, Y. Shen, H. Zhou, Q. Chen, Y. Yang and M. Wang, *Nano Lett.*, 2015, **15**, 2402–2408.
24 H. Wang, X. Hu and H. Chen, *RSC Adv.*, 2015, **5**, 30192–30196.
25 K. Cao, J. Cui, H. Zhang, H. Li, J. Song, Y. Shen, Y. Cheng and M. Wang, *J. Mater. Chem. A*, 2015, **3**, 9116–9122.
26 H. Li, K. Cao, J. Cui, S. Liu, X. Qiao, Y. Shen and M. Wang, *Nanoscale*, 2016, **8**, 6379–6385.
27 H. Chen, Z. Wei, H. He, X. Zheng, K. S. Wong and S. Yang, *Adv. Energy Mater.*, 2016, **6**, 1502087.
28 C.-Y. Chan, Y. Wang, G.-W. Wu and E. W.-G. Diau, *J. Mater. Chem. A*, 2016, **4**, 3872–3878.
29 M. Birkholz, in *Thin Film Analysis by X-Ray Scattering*, Wiley-VCH, KGaA, Germany, 2006, pp. 183–237.
30 L. Zheng, Y. Ma, S. Chu, S. Wang, B. Qu, L. Xiao, Z. Chen, Q. Gong, Z. Wu and X. Hou, *Nanoscale*, 2014, **6**, 8171–8176.
31 Y. Zhou, M. Yang, A. L. Vasiliev, H. F. Garces, Y. Zhao, D. Wang, S. Pang, K. Zhu and N. P. Padture, *J. Mater. Chem. A*, 2015, **3**, 9249–9256.
32 Y. Liu, Z. Yang, D. Cui, X. Ren, J. Sun, X. Liu, J. Zhang, Q. Wei, H. Fan, F. Yu, X. Zhang, C. Zhao and S. F. Liu, *Adv. Mater.*, 2015, **27**, 5176–5183.

33 O. Malinkiewicz, A. Yella, Y. H. Lee, G. M. Espallargas, M. Graetzel, M. K. Nazeeruddin and H. J. Bolink, *Nat. Photonics*, 2013, **8**, 128–132.
34 P. Docampo, F. C. Hanusch, N. Giesbrecht, P. Angloher, A. Ivanova and T. Bein, *APL Mater.*, 2014, **2**, 081508.
35 J. A. Koza, J. C. Hill, A. C. Demster and J. A. Switzer, *Chem. Mater.*, 2016, **28**, 399–405.
36 V. D'Innocenzo, A. R. SrimathKandada, M. De Bastiani, M. Gandini and A. Petrozza, *J. Am. Chem. Soc.*, 2014, **136**, 17730–17733.
37 G. Xing, N. Mathews, S. Sun, S. S. Lim, Y. M. Lam, M. Grätzel, S. Mhaisalkar and T. C. Sum, *Science*, 2013, **342**, 344–347.
38 S. D. Stranks, V. M. Burlakov, T. Leijtens, J. M. Ball, A. Goriely and H. J. Snaith, *Phys. Rev. Appl.*, 2014, **2**, 034007.
39 Y. Yamada, T. Nakamura, M. Endo, A. Wakamiya and Y. Kanemitsu, *J. Am. Chem. Soc.*, 2014, **136**, 11610–11613.
40 H. Y. Hsu, C. Y. Wang, A. Fathi, J. W. Shiu, C. C. Chung, P. S. Shen, T. F. Guo, P. Chen, Y. P. Lee and E. W.-G. Diau, *Angew. Chem., Int. Ed. Engl.*, 2014, **53**, 9339–9342.
41 C. Wehrenfennig, G. E. Eperon, M. B. Johnston, H. J. Snaith and L. M. Herz, *Adv. Mater.*, 2014, **26**, 1584–1589.
42 A. Marchioro, J. Teuscher, D. Friedrich, M. Kunst, R. van de Krol, T. Moehl, M. Grätzel and J.-E. Moser, *Nat. Photonics*, 2014, **8**, 250–255.